

# Lattice Boltzmann simulation on liquid flow and mass transport in a bioreactor with cylinder bundle for hydrogen production

Qiang Liao · Yan-Xia Yang · Xun Zhu ·  
 Hong Wang · Yu-Dong Ding

Received: 27 March 2012 / Accepted: 11 November 2014 / Published online: 25 November 2014  
 © Springer-Verlag Berlin Heidelberg 2014

**Abstract** The lattice Boltzmann method is adopted to simulate hydrodynamics and mass transfer accompanying with biochemical reaction in a channel with cylinder bundle, which is the scenario of biohydrogen production by photosynthetic bacteria in the biofilm attached on the surface of cylinder bundle in photobioreactor. The effects of cylinder spacing, Reynolds number and cylinder arrangement are investigated. The numerical results reveal that highest glucose concentration and the lowest hydrogen concentration are obtained at the front of the first row cylinders for all cases. The staggered arrangement leads to an increment in average drag coefficient, Sherwood number and consumption efficiency of substrate under a given condition, and the increment in Sherwood number reaches up to 30 %, while that in drag coefficient is around 1 %, moreover, the increment in consumption efficiency reaches the maximum value of 12 %. The results indicate that the staggered arrangement is beneficial to the mass transfer and biochemical reaction.

## List of symbols

$c$	Lattice speed ( $\text{m s}^{-1}$ )
$C_x$	Cell density ( $\text{kg m}^{-3}$ )
$D$	Cylinder diameter (m)
$D_\sigma$	Diffusivity coefficient of $\sigma$ -species ( $\text{m}^2 \text{s}^{-1}$ )
$C_D$	Drag coefficient
$\mathbf{e}_i$	Discrete particle velocity in LBE model ( $\text{m s}^{-1}$ )

Q. Liao (✉) · Y.-X. Yang · X. Zhu · H. Wang · Y.-D. Ding  
 Key Laboratory of Low-Grade Energy Utilization Technologies  
 and Systems, Chongqing University, Chongqing 400030, China  
 e-mail: lqzx@cqu.edu.cn

Q. Liao · Y.-X. Yang · X. Zhu · H. Wang · Y.-D. Ding  
 Institute of Engineering Thermophysics, Chongqing University,  
 Chongqing 400030, China

$f_i, f_i^{eq}$	Density distribution function and corresponding equilibrium distribution function of the $i$ th discrete velocity
$f_i^+(\mathbf{x}_w, t)$	Post-collision distribution function at the node $\mathbf{x}_w$
$\overline{f_i^{eq}}(\mathbf{x}_w)$	Approximated equilibrium part at the node $\mathbf{x}_w$
$\mathbf{F}$	The total force acted on the fluid by the solid body ( $\text{J m}^{-1}$ )
$g_{i,\sigma}, g_{i,\sigma}^{eq}$	Concentration distribution function and corresponding equilibrium distribution function of $\sigma$ -species
$J_0$	Rest fraction
$J_{i,\sigma}, K_i$	Specially chosen constants
$k_s$	Monod constant ( $\text{kg m}^{-3}$ )
Ma	Mach number
$p$	Fluid pressure (Pa)
Pe	Peclet number
Re	Reynolds number
$r_\sigma$	React rate of $\sigma$ -species ( $\text{kg m}^{-3} \text{s}^{-1}$ )
$R_\sigma$	Dimensionless react source term of $\sigma$ -species
Sc	Schmidt number
Sh	Sherwood number
$t$	Time (s)
$\mathbf{u}$	Flow velocity ( $\text{m s}^{-1}$ )
$\overline{\mathbf{u}}_w$	Approximation of velocity at node $\mathbf{x}_w$ ( $\text{m s}^{-1}$ )
$s_1, s_2$	Horizontal and vertical cylinder spacings (m)
$S_1, S_2$	Dimensionless horizontal and vertical cylinder spacings
$\mathbf{x}$	Cartesian position vector (m)
$Y_{x/s}$	Cell yield

## Greek letters

$\alpha$	Specific area ( $\text{m}^{-1}$ )
$\Delta$	Fraction of the intersected link in the fluid region, $\Delta =  \mathbf{x}_f - \mathbf{x}_b / \mathbf{x}_f - \mathbf{x}_w $

$\delta_t$	Time space (s)
$\delta_x$	Lattice space (m)
$\nu$	Kinematical viscosity ( $\text{m}^2 \text{s}^{-1}$ )
$\rho$	Flow density ( $\text{kg m}^{-3}$ )
$\overline{\rho_w}$	Approximation of density at the node $\mathbf{x}_w$ ( $\text{kg m}^{-3}$ )
$\tau_\nu$	Dimensionless relaxation time
$\tau_\sigma$	Dimensionless relaxation time related to the diffusion coefficient
$w_i$	Weight coefficient
$\mu_{\max}$	Maximum specific growth rate ( $\text{s}^{-1}$ )
$\eta$	Substrate consumption efficiency per cylinder's surface

## 1 Introduction

Hydrogen, as a clean and renewable energy source as well as an efficient energy carrier with high caloric value ( $122 \text{ kJ g}^{-1}$ ) [1], has a promising potential for replacement of fossil fuels in coming future. Among various hydrogen production methods, biological hydrogen production including dark-fermentation and photo-fermentation has been recognized as an eco-friendly hydrogen production technology [2], owing to its intrinsic advantages over conventional physicochemical approaches, such as low production costs, less pollutant discharge and energy consumption, particularly the capability of providing dual environmental benefits of wastewater treatment and energy generation. Generally, compared with dark-fermentation of carbohydrate-rich wastes, the photo-fermentation of organic acid-rich wastewaters by photosynthetic bacteria (PSB) is favored due to its high purity hydrogen production and high theoretical substrate conversion efficiency. Furthermore, PSB has capabilities of consumption of short-chain organic acids generated from dark-fermentation and trapping light energy over a wide spectral range (from 400 to 900 nm) [3].

Recently, immobilized technology has been introduced to the photo-fermentation bioreactor, and it has been demonstrated that photobioreactor with immobilized cell has high hydrogen production rate over that with suspended cultures, considering its high concentration of biomass and low biomass washout [4]. Currently, the immobilization technologies are branched into granulation and biofilm attachment methods. Unfortunately, granulation immobilization has some obvious weaknesses, such as insufficient use of solar energy and mass transfer limitation of substrates and products [5]. In view of the above mentioned facts, biofilm attachment process is considered as a high-efficient technology for PSB hydrogen production.

To explore the effects of substrate species and operational conditions on substrate biodegradation and hydrogen

production performance of photobioreactor, numerous of experiments had been carried out by researchers [6–8]. However, the time-consuming of experimental techniques and limitations of even high-end measuring equipment make it difficult to gain detailed understanding of the fluid flow, mass transportation and biological reaction that happen during the hydrogen production process in the bioreactor. Consequently, numerical simulations, as useful and powerful approaches, have been widely applied to analyze and predict characteristics of the bioreactor. Some representative numerical models, such as two phase mixture model and reaction kinetic model, were applied in simulation of pollutant biodegradation and mass transport in bioreactor [9, 10]. Unfortunately, these numerical researches are generally restricted to studies on macro-scale, which are difficult to solve the nonlinear partial differential equations. Therefore, some specific assumptions and simplifications, such as multiphase flow simplified as mixed phase and the simplification of interface properties, have to be made for different physical problems, leading to deviating from the real situation and not objectively reflecting the realistic characters to a certain extent. Additionally, these traditional numerical methods have difficulties in obtaining a good numerical stability and high numerical accuracy for complex boundary conditions, such as irregular geometry and moving boundary.

Over the past decades, lattice Boltzmann method (LBM) has emerged as an efficient computational tool on mesoscopic scale with the ability to solve the difficulties that conventional methods cannot deal with. In comparison with conventional numerical methods, a major advantage of LBM is the capability of complex boundary treatment with little additional computational effort [11]. In LB simulation, the evolution of collision and streaming steps of discrete fluid particles is performed on particle distribution functions on mesoscopic scale to simulate the fluid flow. Subsequently, the macroscopic flow properties, such as flow density and velocity, can be determined via these distribution functions. Because of the appealing features, the LBM has attracted increasing attention of academic groups and individuals [12, 13]. Recently, various LB models have been developed ranging from hydrodynamics to heat and mass transport, such as simulations on suspension flow [14, 15], multiphase flow [16–18], micro-flow [19, 20], flow and heat transfer [21, 22], mass transfer [23–25] and chemical reaction [26, 27]. It should be pointed that the mass transfer and reaction are inherently coupled with hydrodynamics in various applications. Unfortunately, some researches for complex coupling system are only on chemical reaction [28, 29]. The application of LBM on bioreaction system has been scarcely reported, particularly combined with complex boundaries, such as curved boundary. Furthermore, it has to point out that the simulation with LBM is a time-consuming process.

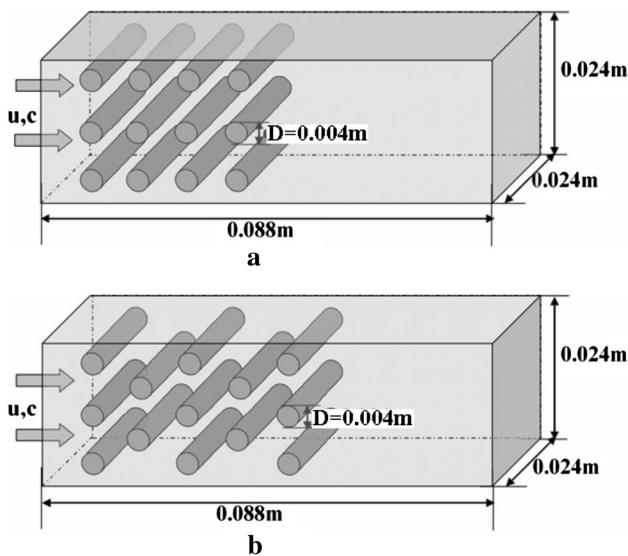


**Fig. 1** Bioreactor installed with **a** inline and **b** staggered cylinder bundle

In the present study, a two-dimensional LB simulation is implemented to explore the coupling hydrodynamics and mass transfer in a biofilm photobioreactor, where cylinder bundle is installed with a certain arrangement and a uniform layer of PSB biofilm is formed on the surface of curved cylinder bundle to degrade the organic compounds, as shown in Fig. 1. The flow and concentration fields are simulated and the effects of cylinder spacing, cylinder bundle arrangement and Reynolds number on flow and mass transfer are investigated. The remainder of this paper is organized as follows. The lattice Boltzmann method is briefly reviewed, followed by the curved boundary treatment. Then a two-dimensional lattice Boltzmann model is established for substrate solution flow around inline and staggered cylinder bundle in a channel. Finally, the simulation results are presented and analyzed.

### 2 Lattice Boltzmann method

The lattice Boltzmann method simulates hydrodynamics and mass transport phenomena by tracking the evolution of distribution functions. These distribution functions are governed by the lattice Boltzmann equation (LBE) [30, 31], which is a special discretization form of the continuous Boltzmann equation. In our simulation, two sets of distribution functions  $f_i(\mathbf{x}, t)$ ,  $g_{i,\sigma}(\mathbf{x}, t)$  are used, relating to flow field and concentration field of the  $\sigma$ -species, respectively:

$$f_i(\mathbf{x} + \mathbf{e}_i \delta_t, t + \delta_t) - f_i(\mathbf{x}, t) = -\tau_v^{-1} (f_i(\mathbf{x}, t) - f_i^{eq}(\mathbf{x}, t)) \tag{1}$$

$$g_{i,\sigma}(\mathbf{x} + \mathbf{e}_i \delta_t, t + \delta_t) - g_{i,\sigma}(\mathbf{x}, t) = -\tau_\sigma^{-1} (g_{i,\sigma}(\mathbf{x}, t) - g_{i,\sigma}^{eq}(\mathbf{x}, t)) + J_{i,\sigma} \delta_t R_\sigma \tag{2}$$

where  $\delta_t$  is the time step,  $\tau_v$  and  $\tau_\sigma$  are the single relaxation time of particle corresponding to  $f(x, t)$  and  $g(x, t)$  respectively, and  $R_\sigma$  is the non-dimensional reaction source.  $\mathbf{e}_i$  is the particle velocity vector and in two-dimensional nine-velocity (D2Q9) LB model, it is given by  $\mathbf{e}_0 = 0$ ;  $\mathbf{e}_i = c(\cos \theta_i, \sin \theta_i)$ ,  $\theta_i = (i - 1)\pi/2$ ,  $i = 1-4$ ;  $\mathbf{e}_i = \sqrt{2}c(\cos \theta_i, \sin \theta_i)$ ,  $\theta_i = (i - 1)\pi/2$ ,  $i = 5-8$ .  $f_i^{eq}(\mathbf{x}, t)$  and  $g_{i,\sigma}^{eq}(\mathbf{x}, t)$  are equilibrium distribution functions of  $f(x, t)$  and  $g(x, t)$  at position  $\mathbf{x}$  and time  $t$ , expressed as [28]:

$$f_i^{eq}(\mathbf{x}, t) = w_i \rho \left[ 1 + \frac{3\mathbf{e}_i \cdot \mathbf{u}}{c^2} + \frac{9(\mathbf{e}_i \cdot \mathbf{u})^2}{2c^4} - \frac{3\mathbf{u}^2}{2c^2} \right], \quad i = 0, \dots, 8 \tag{3}$$

$$g_{i,\sigma}^{eq}(\mathbf{x}, t) = c_\sigma \left( J_{i,\sigma} + K_i \frac{\mathbf{e}_i \cdot \mathbf{u}}{c^2} \right), \quad i = 0, \dots, 4 \tag{4}$$

where  $c$  is the lattice speed and defined as  $c = \delta_x / \delta_t$  with lattice space  $\delta_x$ , and the sound speed of the model is represented as  $c_s = c / \sqrt{3}$ . In Eq. (3), the weight coefficients  $w_i$  are given by  $w_0 = 4/9$ ;  $w_i = 1/9$ ,  $i = 1-4$ ;  $w_i = 1/36$ ,  $i = 5-8$ . In Eq. (4),  $J_{i,\sigma}$  and  $K_i$  are specially chosen constants and determined by  $J_{i,\sigma} = \begin{cases} J_0, & i = 0 \\ (1 - J_0)/4, & i = 1-4 \end{cases}$ ,  $K_i = 1/2$ , where the rest fraction  $J_0$  can be selected from 0 to 1 [28, 29].

On macro-level, the fluid density  $\rho$ , velocity  $\mathbf{u}$  and concentration of  $\sigma$ -species  $c_\sigma$  are evaluated in terms of particle distribution functions:

$$\rho = \sum_{i=0}^8 f_i(\mathbf{x}, t) \tag{5}$$

$$\rho \mathbf{u} = \sum_{i=0}^8 \mathbf{e}_i f_i(\mathbf{x}, t) \tag{6}$$

$$c_\sigma = \sum_{i=0}^4 g_{i,\sigma}(\mathbf{x}, t) \tag{7}$$

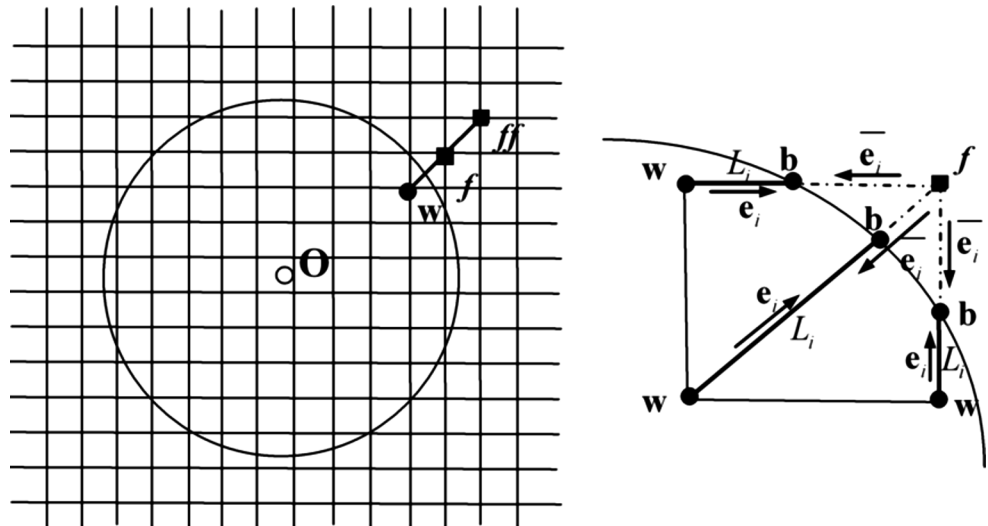
By performing the Chapman–Enskog expansion on Eqs. (1, 2) in the incompressible limit  $Ma = |\mathbf{u}|/c_s \ll 1$ , both the Navier–Stokes equation and mass transfer equation can be recovered as [32, 33]:

$$\begin{cases} \nabla \cdot \mathbf{u} = 0 \\ \partial_t \mathbf{u} + \nabla \mathbf{u} \mathbf{u} = -\nabla p + \nu \nabla^2 \mathbf{u} \end{cases} \tag{8}$$

$$\partial_t c_\sigma + \mathbf{u} \nabla c_\sigma - D_\sigma \nabla^2 c_\sigma = r_\sigma \tag{9}$$

where the pressure  $p$  satisfies the state equation  $p = \rho c_s^2$ , and the viscosity and diffusivity are represented as  $\nu = \delta_t c_s^2 (\tau - 1/2)$  [34] and  $D_\sigma = \delta_t c^2 C_Q (1 - J_0) (\tau_\sigma - 1/2)$  with  $C_Q = 1/2$  [28].

**Fig. 2** Layout of the regularly spaced lattices and curved wall boundary



### 3 Treatment for curved boundary

#### 3.1 Treatment of curved boundary condition

Boundary treatment is a key step for the LB simulation. For the curved wall boundary shown in the present simulation, a non-equilibrium extrapolation method [35] with second-order accuracy is chosen to deal with the curved boundary.

As shown in Fig. 2, the link between the wall node  $\mathbf{x}_w$  and fluid node  $\mathbf{x}_f$  ( $\mathbf{x}_f = \mathbf{x}_w + \mathbf{e}_i \delta_t$ ) intersects the physical boundary at  $\mathbf{x}_b$ . The fraction of the intersected link in the fluid region is  $\Delta = |\mathbf{x}_f - \mathbf{x}_b|/|\mathbf{x}_f - \mathbf{x}_w|$ ,  $0 \leq \Delta \leq 1$ . If the distance  $L_i$  between nodes  $\mathbf{x}_w$  and  $\mathbf{x}_b$  satisfies the rules:  $L_i < \delta_x$ ,  $i = 1-4$ ;  $L_i < \sqrt{2}\delta_x$ ,  $i = 5-8$ , the non-equilibrium extrapolation needs to be enforced on  $i$ th at node  $\mathbf{x}_w$  to obtain the distribution function  $f_i^+(\mathbf{x}_w, t)$ , and then the streaming step  $f_i(\mathbf{x}_f, t + \delta_t) = f_i^+(\mathbf{x}_w, t)$  for fluid node  $\mathbf{x}_f$  can be finished [36].

In the non-equilibrium extrapolation method [35], the distribution function at wall node  $\mathbf{x}_w$  is decomposed into equilibrium and non-equilibrium parts:

$$f_i(\mathbf{x}_w, t) = f_i^{\text{eq}}(\mathbf{x}_w, t) + f_i^{\text{ne}}(\mathbf{x}_w, t) \tag{10}$$

The equilibrium part is approximated by a fictitious one  $\bar{f}_i^{\text{eq}}(\mathbf{x}_w, t)$  and is given by:

$$\bar{f}_i^{\text{eq}}(\mathbf{x}_w, t) = \omega_i \bar{\rho}_w \left( 1 + \frac{3(\mathbf{e}_i \cdot \bar{\mathbf{u}}_w)}{c^2} + \frac{9(\mathbf{e}_i \cdot \bar{\mathbf{u}}_w)^2}{2c^4} - \frac{3\bar{\mathbf{u}}_w^2}{2c^2} \right) \tag{11}$$

where  $\bar{\rho}_w = \rho(\mathbf{x}_f)$  is an approximation of density,  $\bar{\mathbf{u}}_w$  an approximation of fluid velocity determined via linear extrapolation of neighboring fluid nodes  $\mathbf{x}_f, \mathbf{x}_{ff}$  ( $\mathbf{x}_{ff} = \mathbf{x}_f + \mathbf{e}_i \delta_t$ ):

$$\begin{cases} \Delta \geq 0.75, \bar{\mathbf{u}}_w = \mathbf{u}_{w1} \\ \Delta < 0.75, \bar{\mathbf{u}}_w = \Delta \mathbf{u}_{w1} + (1 - \Delta) \mathbf{u}_{w2} \end{cases} \tag{12}$$

where  $\mathbf{u}_{w1} = [\mathbf{u}(\mathbf{x}_b) + (\Delta - 1)\mathbf{u}(\mathbf{x}_f)]/\Delta$ ,  $\mathbf{u}_{w2} = [2\mathbf{u}(\mathbf{x}_b) + (\Delta - 1)\mathbf{u}(\mathbf{x}_{ff})]/(\Delta + 1)$ .

In order to be consistent with the definition of  $\bar{\mathbf{u}}_w$ , the non-equilibrium part of the distribution function is also determined by linear extrapolation of neighboring fluid nodes  $\mathbf{x}_f, \mathbf{x}_{ff}$  proposed by Guo [35]:

$$\begin{cases} \Delta \geq 0.75, f_i^{\text{ne}}(\mathbf{x}_w, t) = f_i^{\text{ne}}(\mathbf{x}_f, t) \\ \Delta < 0.75, f_i^{\text{ne}}(\mathbf{x}_w, t) = \Delta f_i^{\text{ne}}(\mathbf{x}_f, t) + (1 - \Delta) f_i^{\text{ne}}(\mathbf{x}_{ff}, t) \end{cases} \tag{13}$$

Finally, the post-collision distribution function  $f_i^+(\mathbf{x}_w, t)$  can be obtained as:

$$f_i^+(\mathbf{x}_w, t) = \bar{f}_i^{\text{eq}}(\mathbf{x}_w, t) + (1 - \tau_v^{-1}) f_i^{\text{ne}}(\mathbf{x}_w, t) \tag{14}$$

Similarly, based on the fraction of the intersected link in the fluid region  $\Delta$ , the concentration distribution function at node  $\mathbf{x}_w$  can be obtained by interpolation of the neighboring fluid nodes  $\mathbf{x}_f, \mathbf{x}_{ff}$ . One can refer literature [37] for more details.

#### 3.2 Force evaluation on a solid body

There are two approaches to evaluate force in lattice Boltzmann method: stress integration [38] and momentum exchange [39]. Compared with stress integration approach, the momentum exchange method is more reliable, more accurate and easier to implement for complex boundary. Hence, the momentum exchange method is employed to evaluate the force on the curved cylinder surfaces.

The momentum exchange occurs during the subsequent streaming step when  $f_i^+(\mathbf{x}_w, t)$  and  $f_i^+(\mathbf{x}_f, t)$  move to  $\mathbf{x}_f$  and  $\mathbf{x}_w$ , respectively. For a given boundary node  $\mathbf{x}_w$ , the momentum exchange with all possible neighboring fluid nodes over a time step  $\delta_t$  is [39]:

$$\sum_{i \neq 0} \bar{\mathbf{e}}_i \left[ f_i^+(\mathbf{x}_f, t) + f_i^+(\mathbf{x}_w, t) \right] [1 - w(\mathbf{x}_w + \mathbf{e}_i \delta_t)] \delta_x^2 \quad (15)$$

where  $\bar{\mathbf{e}}_i$  denotes the velocity vector in the opposite direction,  $\bar{\mathbf{e}}_i = -\mathbf{e}_i$ .  $w(\mathbf{x})$  is a scalar array, with  $w(\mathbf{x}) = 0$  for lattice node occupied by fluid, and  $w(\mathbf{x}) = 1$  for lattice node inside the solid body.

Come to this fax, the total force exerted on the solid body can be obtained by summing the contribution over all boundary nodes  $\mathbf{x}_w$ , belonging to the body [39]:

$$\mathbf{F} = \sum_{\text{all } \mathbf{x}_w} \sum_{i \neq 0} \bar{\mathbf{e}}_i \left[ f_i^+(\mathbf{x}_f, t) + f_i^+(\mathbf{x}_w, t) \right] [1 - w(\mathbf{x}_w + \mathbf{e}_i \delta_t)] \delta_x^2 / \delta_t \quad (16)$$

where the value of  $f_i^+(\mathbf{x}_w, t)$  at the boundary can be obtained by Eq. (14).

#### 4 Numerical simulation

The lattice Boltzmann model validated in our previous study [37] is applied to simulate the hydrodynamics and mass transport presented in the process of substrate degradation and hydrogen production by PSB in a thin biofilm on the surface of cylinder bundle, as shown in Fig. 1. For this scenario, the simplifying assumptions are set as following:

1. A steady-state biofilm is formed on the surface of cylinder bundle.
2. In the bioreactor, the bacteria are mainly concentrated in the biofilm attached on the surface of cylinders, and the bacteria in the bulk flow are very few. Therefore, the bioreaction in the bulk flow is neglected.
3. The biochemical reaction only occurs on the surface of cylinders due to such thin biofilm compared with the cylinder's diameter.
4. The heat released from biochemical reaction is small enough to be neglected and hence brings no effect on the flow field.
5. The main component of the substrate solution is glucose and the main product of the biodegradation is hydrogen based on previous study in our group.
6. The produced hydrogen is completely dissolved in solution considering the rather small amount of produced hydrogen, which also consists with the observation in the experiments.
7. The physical properties of substrate and product are assumed to be invariant during biochemical reaction due to rather small amount of degradation.

The substrate consumption rate  $r_1$  ( $\text{C}_6\text{H}_{12}\text{O}_6$ ) and hydrogen production rate  $r_2$  ( $\text{H}_2$ ) by PSB in biofilm can be described by Obeid et al. [40]:

$$r_1 = \frac{C_x \cdot \mu_{\max} \cdot c_1}{Y_{x/s} \cdot (k_s + c_1)}, \quad r_2 = \alpha \frac{1}{Y_{x/s}} \frac{\mu_{\max} \cdot c_1 \cdot C_x}{(k_s + c_1)} \quad (17)$$

where  $C_x$ ,  $\mu_{\max}$ ,  $Y_{x/s}$ ,  $k_s$ ,  $\alpha$  are cell density, maximum specific growth rate, cell yield, Monod constant and growth associated kinetic constant for hydrogen production with values of  $0.76 \text{ kg m}^{-3}$ ,  $7.218 \times 10^{-5} \text{ s}^{-1}$ ,  $0.847$ ,  $5.204 \text{ kg m}^{-3}$  and  $0.0192$ , respectively.  $c_1$  is the local substrate concentration.

Figure 3 shows the schematic illustration of physical models of glucose solution flow around the cylinder bundle with PSB biofilm for biohydrogen production. To investigate the effect of bundle arrangement, inline (Fig. 3a) and staggered (Fig. 3b) cylinder bundle are set corresponding to the bioreactors in Fig. 1a, b, respectively. As shown in Fig. 3, the two-dimensional simulation channel is of size  $22D \times 6D$ , and the upstream inlet is set as 2.5 times of cylinder diameter away from the front row of cylinders. The bottom and top walls are both set as 0.5 times of cylinder spacing away from the nearby cylinders.  $s_1$ ,  $s_2$  represent the horizontal and vertical cylinder spacing, respectively, and it is specified that  $s_1 = s_2 = s$ . In order to understand the effect of cylinder spacing on the flow and mass transport, various cylinder spacings ( $s = 1.5D, 2.0D, 3.0D$ ) are set in the simulations.

Convenient for generalization and analysis, normalizations are conducted using the cylinder diameter  $D$ , mean inlet fluid velocity  $\bar{u}$  and inlet fluid concentration  $c_0$ , and hence a set of dimensionless variables is expressed as:

$$X = x/D, \quad Y = y/D, \quad S = s_1/D = s_2/D, \\ U_x = u_x/\bar{u}, \quad U_y = u_y/\bar{u}, \quad C_\sigma = c_\sigma/c_0 \quad (18)$$

The dimensionless reaction source terms are defined by:

$$R_1 = \frac{r_1 D}{c_0 \bar{u}}, \quad R_2 = \frac{r_2 D}{c_0 \bar{u}} \quad (19)$$

The dimensionless parameters, Reynolds number, Schmidt number and Peclet number, used to characterize the hydrodynamics and mass transport are given as:

$$\text{Re} = \bar{u}D/\nu, \quad \text{Sc} = \nu/D_\sigma, \quad \text{Pe} = \text{ReSc} \quad (20)$$

For the cases simulated in the present study, the Schmidt number for the substrate flow is  $\text{Sc}_1 = 476$  and for the product flow is  $\text{Sc}_2 = 267$ . Furthermore, the boundary conditions of macroscopic variables are set as following:

Inlet boundary conditions:  $U_x = 4U_{\max}Y(H - Y)/H^2$ ,

$U_y = 0$ ,  $C_1 = 1.0$ ,  $C_2 = 0.0$ .

Outlet boundary conditions:  $\frac{\partial U_x}{\partial X} = 0$ ,  $\frac{\partial U_y}{\partial X} = 0$ ,  $\frac{\partial C_\sigma}{\partial X} = 0$ .

Boundary conditions at the bottom and top walls:  $U_x = 0$ ,

$U_y = 0$ ,  $\frac{\partial C_\sigma}{\partial Y} = 0$ .

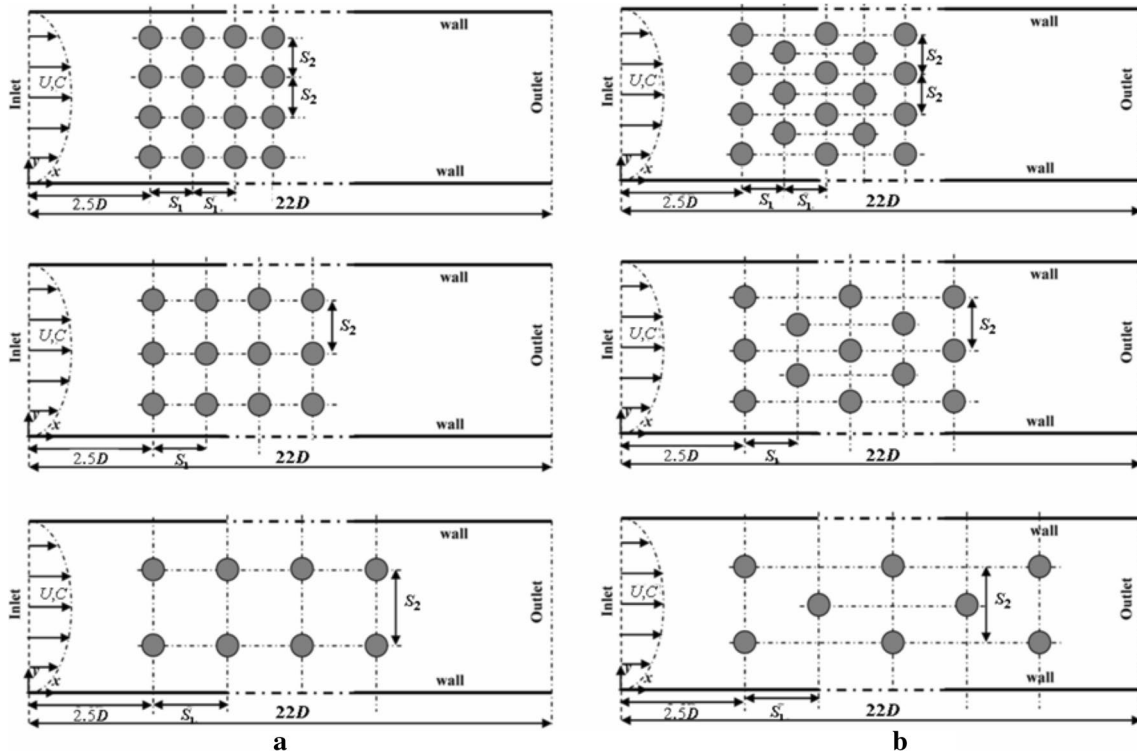


**Fig. 3** Schematic of fluid flow around **a** inline and **b** staggered cylinder bundle in a channel

Boundary conditions at solid surface of the cylinder:  
 $U_x = 0, \quad U_y = 0, \quad Q_{diffusion} = Q_{reaction}.$

The lattice Boltzmann model with the treatment of curved boundary conditions has been validated in our previous work [37]. When the grid density  $D/\delta_x = 20$ , the numerical results have a good agreement with the benchmark data [41]. Moreover, references [42–44] also demonstrated that choosing the grid density  $D/\delta_x = 20$  results in a good accuracy. Hence in present study, the grid density is set  $D/\delta_x = 20$ , and the simulation is performed in a uniform mesh  $N_x \times N_y = 441 \times 121$ . In order to estimate the flow and mass transfer during the substrate degradation and hydrogen generation, the drag coefficient  $C_D$ , Sherwood number  $Sh$  and consumption efficiency  $\eta$  of the substrate flow are introduced. The drag coefficient is defined by  $C_D = F_x / (\frac{1}{2} \rho_0 \bar{u}^2 D)$ , where drag force  $F_x$  is the  $x$ -component of  $\mathbf{F}$  obtained by Eq. (16). The mass transfer analog of the Nusselt number in heat transfer is the Sherwood number ( $Sh$ ). Similar to the definition of  $Nu$  number [22], the  $Sh$  number is expressed as  $Sh = -\frac{1}{360} \int_0^{360} \frac{D}{C_w - C_0} \frac{\partial C}{\partial \mathbf{n}} d\theta$ , where  $C_0, C_w$  are the inlet and wall concentrations,  $\mathbf{n}$  is the outer-normal vector of cylindrical wall, and  $\theta$  is the angle around a cylinder. The substrate consumption efficiency per cylinder’s surface, which can be used to assess the hydrogen production performance in the channel, is calculated as  $\eta = \left( \frac{Q_{in} - Q_{out}}{Q_{in}} \right) \Big|_{substrate} \times 100 \%$ , where  $Q_{in}, Q_{out}$

are the mass flow of inlet and outlet, and  $n$  is the cylinder number.

### 5 Results and discussion

#### 5.1 Fluid flow and mass transfer for glucose solution flow around inline cylinder bundle

The flow and mass transport of glucose solution flow around inline cylinder bundle with various cylinder spacings ( $S = 1.5, 2.0, 3.0$ ) are investigated at different Reynolds numbers. For a given Reynolds number  $Re = 0.14$ , the effect of cylinder spacing on velocity and concentration fields in the channel is presented in Fig. 4. It is easy to note, from Fig. 4a, that the glucose solution smoothly flows around the inline cylinder bundle to form a steady laminar flow with no separation behind cylinders due to low Reynolds number ( $<1$ ) for all cases. However, for a specific inlet flow area, the actual flow path in the channel is significantly compressed at smaller cylinder spacing, say  $S = 1.5$ , which induces a distinctly deformation of the streamlines between the cylinders in a row perpendicular to the flow direction. As a result, the fluid velocity in the centerline between cylinders in two lines is remarkably increased and the flow boundary layer is thinned, hence magnifying velocity gradient around the cylinders. Furthermore, the interaction of

cylinders in the front and back rows is strengthened with decreasing cylinder spacing due to most cylinders right being in wake flow zone from the second row, which also donates to the change of the velocity and pressure profile in the channel. Unfortunately, it should be pointed out that high velocity will go against the biofilm growth, leading to washout of the bacteria. Generally speaking, the flow field has a great impact on concentration fields of the glucose solution and produced hydrogen, as shown in Fig. 4b. With decreasing cylinder spacing, the concentration boundary layer around cylinders is evidently cut thinner due to thinner flow boundary condition, and then severe concentration variation between cylinders in a row is presented for both the substrate and product flow. These result in distinct concentration gradient around cylinders which is beneficial to the mass transfer of substrate and product on the reaction surfaces. Furthermore, another result from the smaller cylinder spacing is the increment in the number of cylinders in the channel, that is, the increment in the bioreaction area. The streaming, diffusion and bioreaction happened in the upstream cylinders with observable change of the flow area are accumulatively impressed on the flow field and mass concentration profile around the downstream cylinders. Therefore, the concentration contours with value smaller than 1.0 for the substrate is shrunk towards inlet and the concentration contours for the product is lengthened towards outlet in the case with smaller cylinder spacing, as a result, lower substrate concentration and higher product concentration are observed at the outlet of the channel.

To avoid washout of the biofilm on the surface of cylinders, low glucose solution flow rate is expected, and thus various Re numbers ( $Re = 0.14, 0.28, 0.56$ ) are set to investigate its effect on flow and mass transfer in the channel where the cylinder spacing is settled as  $S = 2.0$ . It is noted that the solution flow around the cylinder bundle in the channel is still a steady laminar flow with no separation due to all the Re numbers adopted here are lower than 1, and the streamlines under various Re numbers are calculated to be similar to that in the case with  $Re = 0.14$  and  $S = 2.0$  (cf. Fig. 4a). Then, the concentration contours of substrate and product are presented in Fig. 5 for the glucose solution flow around the inline cylinder bundle with cylinder spacing  $S = 2.0$ . Although the impact of Re number on the flow field is slight, differences in concentration contours at various Re numbers are apparently observed. With increasing Re number, the concentration gradient around cylinders increases due to thinned flow boundary layer, and then the substrate diffusion and consumption as well as hydrogen production by the biofilm are enhanced. Meanwhile, the concentration contours is lengthened along X-direction either for the substrate or for the product, presenting higher substrate concentration and lower product concentration downstream the channel at larger Re number.

This can be understood that the total substrate load (defined as the product of inlet substrate concentration and flow rate) is significantly increased with increasing Re number, and its increment is even larger than the increase in the consumption by biofilm resulted from enhanced mass transfer, and therefore the residual glucose is delivered downstream owing to strong convection effect. Similarly, the produced hydrogen is also swiftly delivered out of the channel with fluid flow. For more clarity, the velocity and concentration profiles along the channel centerline at various Re numbers are shown in Fig. 6. It is clear that the flow has reached steady state at the outlet, and the velocity slightly increases with an increase in Re number (cf. Fig. 6a). As expected, the highest substrate concentration as well as the lowest hydrogen concentration appears at the front of cylinders in the first row (cf. Fig. 6b) due to the onset of bioreaction. Afterwards, if one put an eye on the rear of cylinder, the glucose concentration orderly decreases and the hydrogen concentration significantly increases along X-direction owing to the consumption and production of bioreaction by PSB biofilm on the cylinder surface. Additionally, considering the influence from fluid flow, the glucose concentration at the front of cylinders is higher than that at the rear of cylinders, and the hydrogen concentration is reverse to the variation of substrate concentration. Furthermore, the substrate concentration increases while the product concentration decreases with increasing Re number, due to high flow velocity and short hydraulic retention time (HRT).

Based on above calculation results and analysis on the flow and mass transport for glucose solution flow around the inline cylinder bundle, the average drag coefficient  $C_d$ , Sherwood number  $Sh$  and consumption efficiency  $\eta$  of the substrate flow around cylinders are estimated at different Re numbers and cylinder spacings, as shown in Table 1. For the cases with various cylinder spacings, the average drag coefficient, Sherwood number and consumption efficiency of the substrate flow increase with decreasing cylinder spacing at a given Re number. As analyzed for Fig. 4, for the small cylinder spacing, the limitation of flow path between cylinders results in large velocity and concentration gradients, which simultaneously leads to high flow resistance and high mass transfer efficient. This indicates that the improvement of Sherwood number is at the expense of increasing drag coefficient at the small cylinder spacing, and the increment in drag coefficient is found to be boomed with decreasing cylinder spacing due to strong interaction between cylinders of the front and back rows. The enhancement of the substrate consumption efficiency can be attributed to the enhanced mass transfer process. For the cases with various Re numbers, it can be seen that the drag coefficient evidently decreases with an increase in Re number at a given cylinder spacing. This can be understood, if one keeps in mind that the total drag is determined

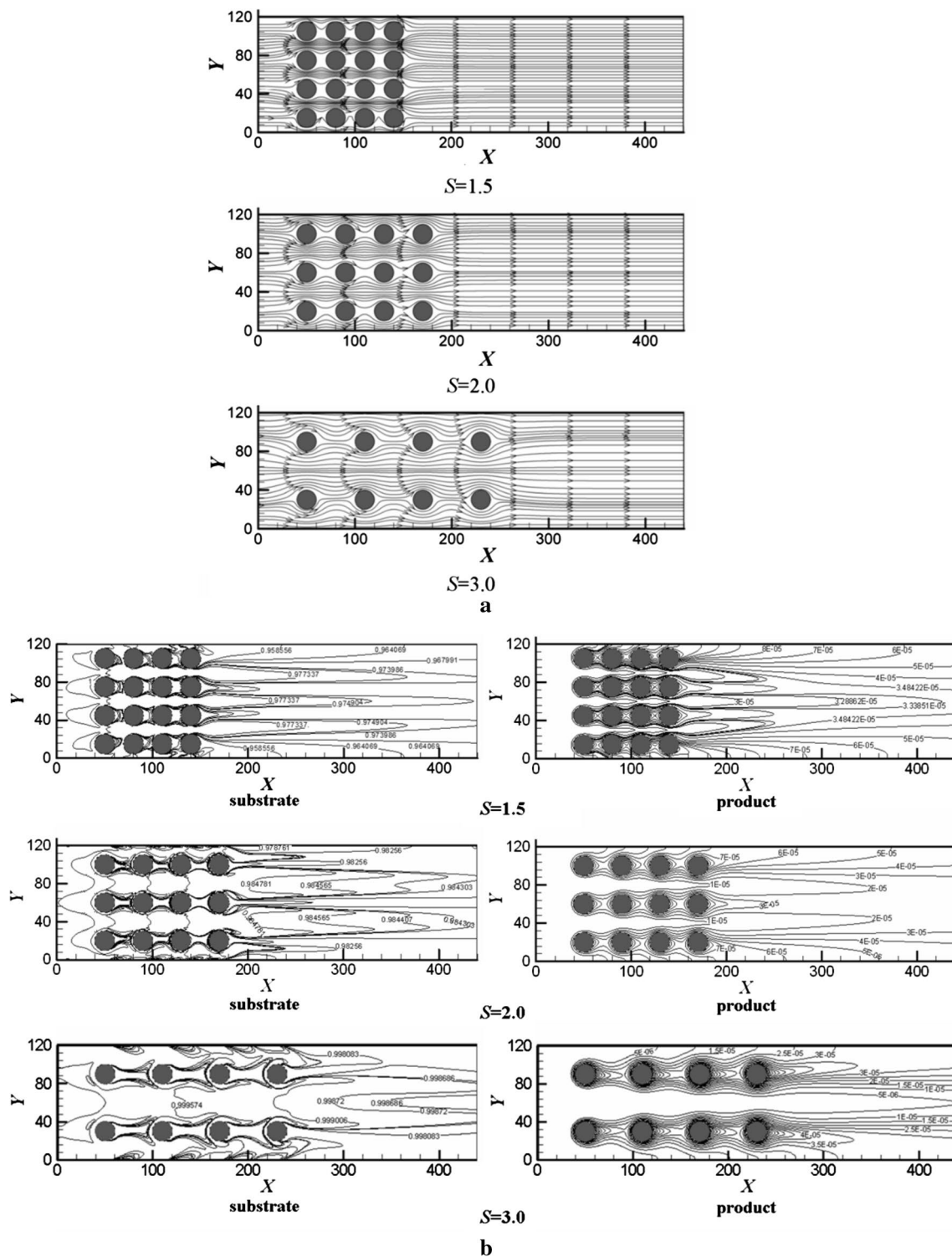


**Fig. 4** **a** Velocity fields and **b** concentration contours of substrate and product of fluid flow around inline cylinder bundle with various cylinder spacings  $S$  in a channel at  $Re = 0.14$

by friction drag and pressure drag, that the friction drag predominates the total drag at low  $Re$  number, while pressure drag increases more significantly with increasing  $Re$

number, hence resulting in the decrease in  $C_d$ . Furthermore, as analyzed for Figs. 5 and 6, with increasing  $Re$  number, the increased substrate load and thinned boundary layer



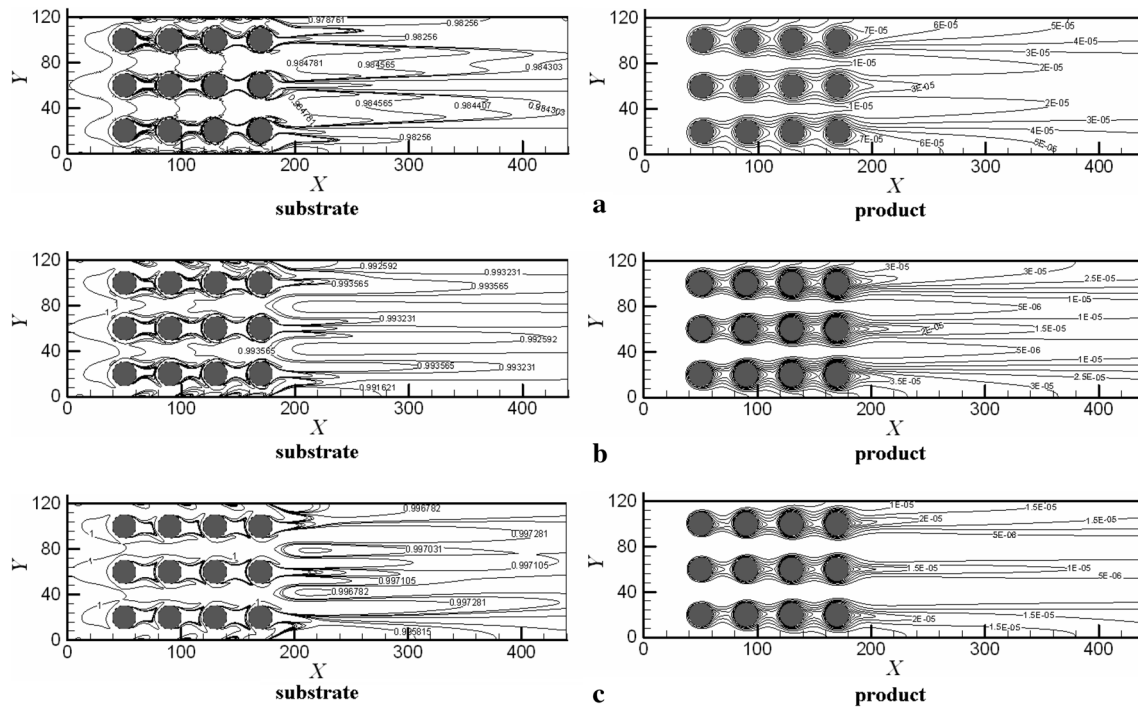


**Fig. 5** Concentration contours of substrate and hydrogen product for fluid flow around inline cylinder bundle with cylinder spacing  $S = 2.0$  for **a**  $Re = 0.14$ , **b**  $Re = 0.28$  and **c**  $Re = 0.56$

accelerate the substrate transfer to the cylinder surfaces for biodegradation, hence improving the average Sherwood number of substrate around cylinders. However, the significantly increment in the inlet substrate load overruns that in the biodegradation, leading to decreasing substrate consumption efficiency.

## 5.2 Fluid flow and mass transfer for glucose solution flow around staggered cylinder bundle

For understanding the effect of bundle arrangement, the flow and mass transport for glucose solution flow around staggered cylinder bundle are also investigated. Similarly, the effect of cylinder spacing and  $Re$  number are discussed, respectively. Figure 7 shows the velocity fields and concentration contours of the substrate and product at various cylinder spacings ( $S = 1.5, 2.0, 3.0$ ) under the condition of  $Re = 0.14$ . Similar to the flow around the inline bundle shown in Fig. 4, the fluid flow around the staggered cylinder bundle still keeps a steady flow with no separation (cf. Fig. 7a). However, a distinct difference from the inline bundle is that the streamlines for the staggered arrangement present a large lateral meander of one half of a cylinder diameter or less. This can be attributed to that each cylinder gets a chance to directly face the coming flow from the gap of cylinders in the front row for the case with staggered arrangement, and this will definitely enhance the

perturbation on the flow field, leading to thinning the flow boundary layer on the cylinders and increasing the velocity gradient. Meanwhile, with increasing cylinder spacing, the interaction of wake flow and coming flow among the cylinders is weakened and then, the streamlines show more smooth (cf. Fig. 7a). Furthermore, the perturbation in flow field also provides an impact on the concentration fields. The concentration contours at the rear of cylinders present a large inclination for both the glucose and produced hydrogen, and the inclination tends to be smooth while the concentration boundary layer tends to be thick with increasing cylinder spacing due to less influence from the flow around upstream cylinders, as seen in Fig. 7b. Compared with the flow in inline bundle (cf. Fig. 4b), the concentration boundary layers of the substrate and produced hydrogen are thinner in the case with staggered cylinder bundle at a given cylinder spacing, implying that the staggered arrangement facilitates the mass transfer on the reaction surfaces. This can be validated by the case with cylinder spacing of 3.0 (cf. Fig. 7b), in which the total number of cylinders is the same as that in the inline bundle case with  $S = 3.0$  (cf. Fig. 4b). It can be found that in the staggered bundle case the substrate concentration is lower while the product concentration is higher than those in the inline bundle case at the same downstream site of the channel.

For glucose solution flow in the staggered cylinder bundle, the effect of  $Re$  number on flow and mass transport are

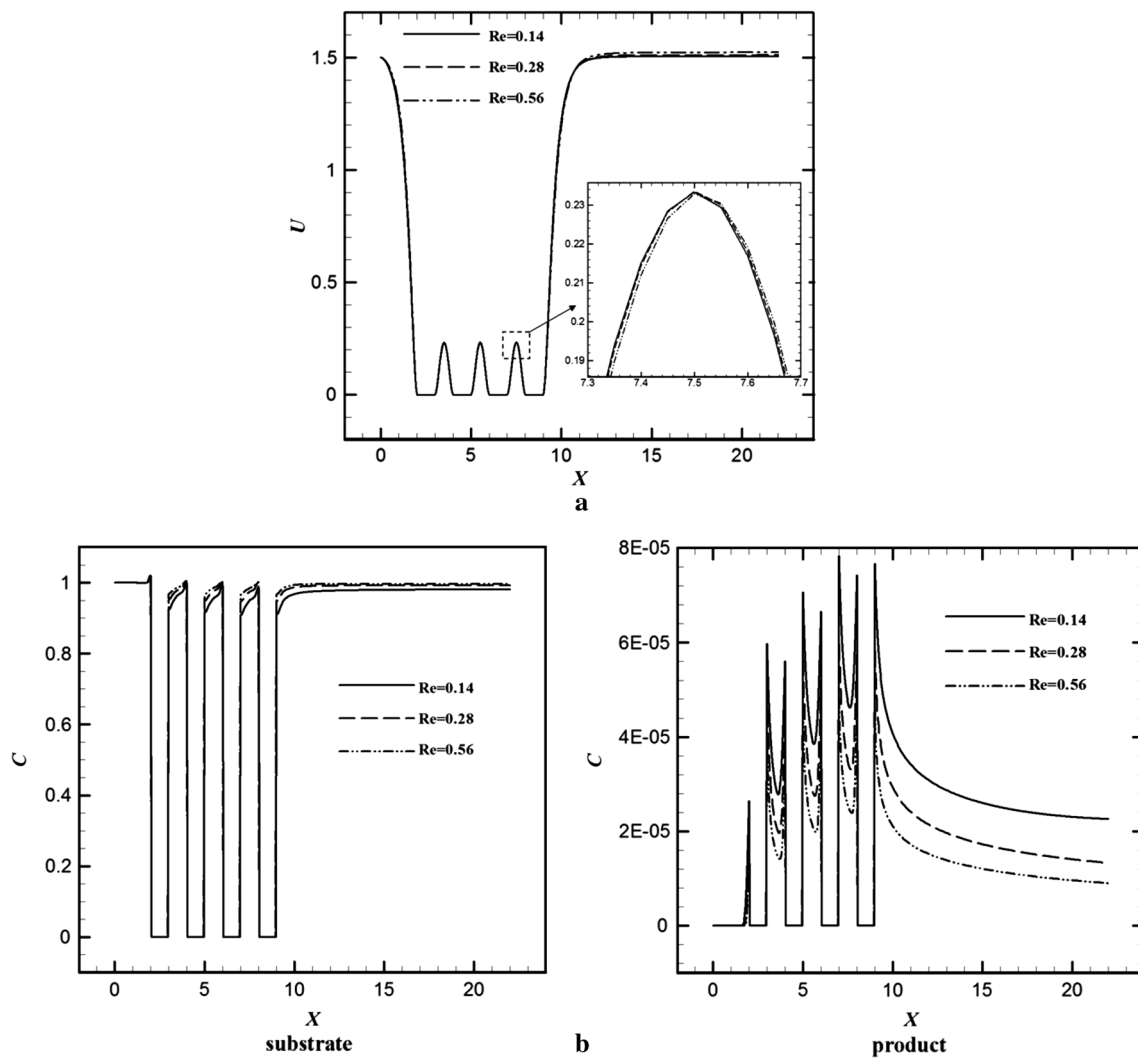


**Fig. 6** Comparison of **a** velocity and **b** concentration profiles along channel centerline of fluid flow around inline cylinder trundles with cylinder spacing  $S = 2.0$  for  $Re = 0.14, 0.28$  and  $0.56$

**Table 1** The effects of  $Re$  number and cylinder spacing  $S$  on drag coefficient, Sherwood number and consumption efficiency of substrate for fluid flow around inline cylinder bundles

$Re$	$C_d$			$Sh$			$\eta$ (%)		
	0.14	0.28	0.56	0.14	0.28	0.56	0.14	0.28	0.56
$S$									
1.5	2,431.65	1,235.42	638.48	0.071	0.124	0.225	0.550	0.506	0.497
2.0	861.34	432.45	218.13	0.034	0.062	0.114	0.511	0.463	0.441
3.0	407.89	204.36	102.71	0.020	0.038	0.071	0.462	0.417	0.407

also studied at a given cylinder spacing  $S = 2.0$ , and various  $Re$  numbers are chosen as  $Re = 0.14, 0.28$  and  $0.56$ . Figure 8 presents the concentration contours of glucose and hydrogen under conditions with various  $Re$  numbers. The concentration boundary layer, either for the substrate or product, almost develops individually on each cylinder at all conditions. As the fluid convection effect is strengthened with an increase in  $Re$  number, the thickness of

concentration boundary layers experiences a minification. It is easy to note, from the comparison of Figs. 5 and 8, that the concentration boundary layer of flow in the staggered bundles is thinner than that of flow in the inline bundles under a given  $Re$  number, which should be attributed to the enhanced perturbation and weakened wake flow resulting in thinner velocity boundary layer. Furthermore, the velocity and concentration profiles along channel

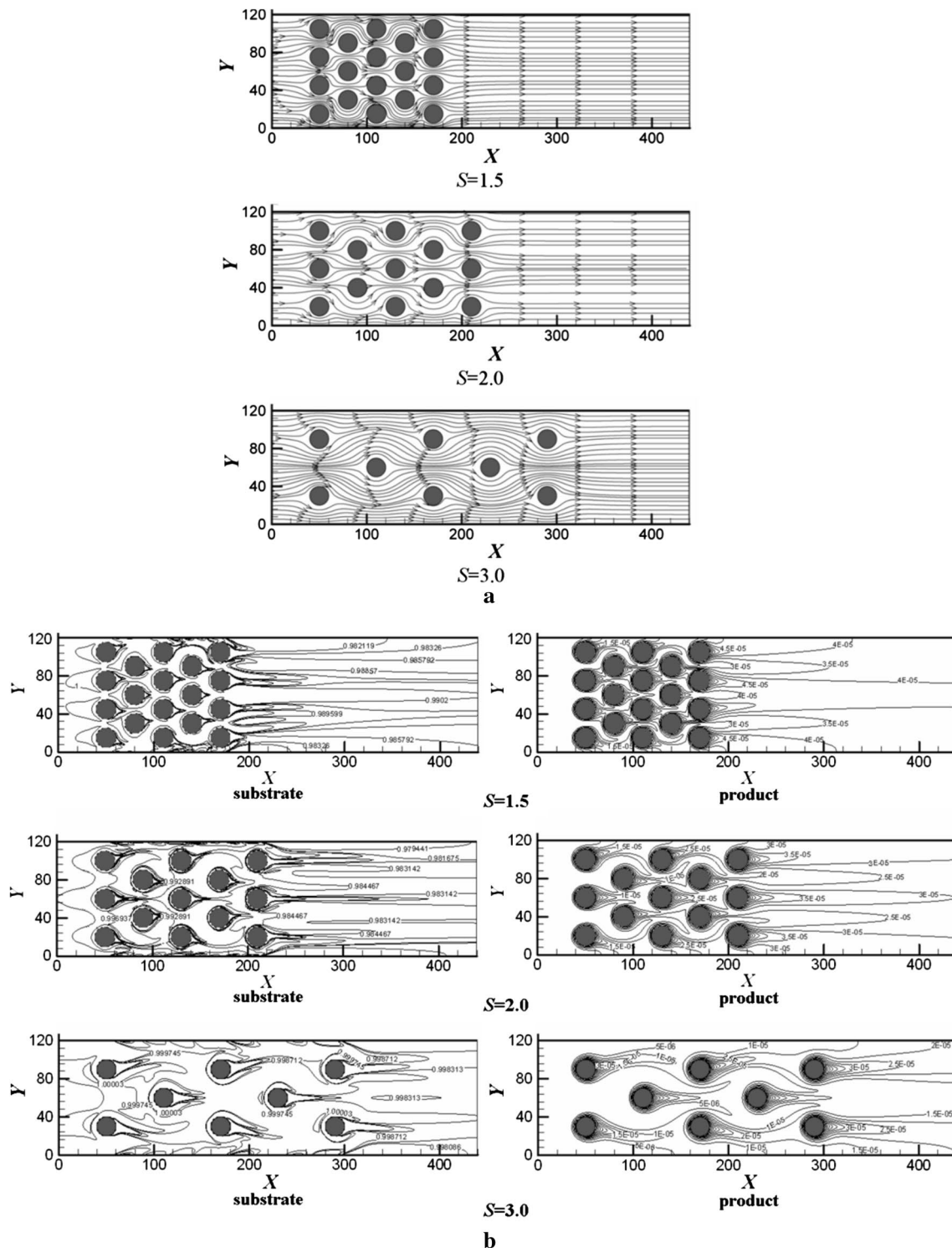


**Fig. 7** **a** Velocity fields and **b** concentration contours of substrate and product of fluid flow around staggered cylinder bundle with various cylinder spacings  $S$  in a channel at  $Re = 0.14$

centerline are presented in Fig. 9. As  $Re$  number is rather low, the difference in velocity for various  $Re$  numbers is very indistinct (cf. Fig. 9a), while the variation in concentrations of the glucose and hydrogen are evident (cf.

Fig. 9b), implying that small fluid disturbance will induce great impact on concentration fields in the bioreactor, especially for the product. The substrate concentration increases while the product concentration decreases with increasing

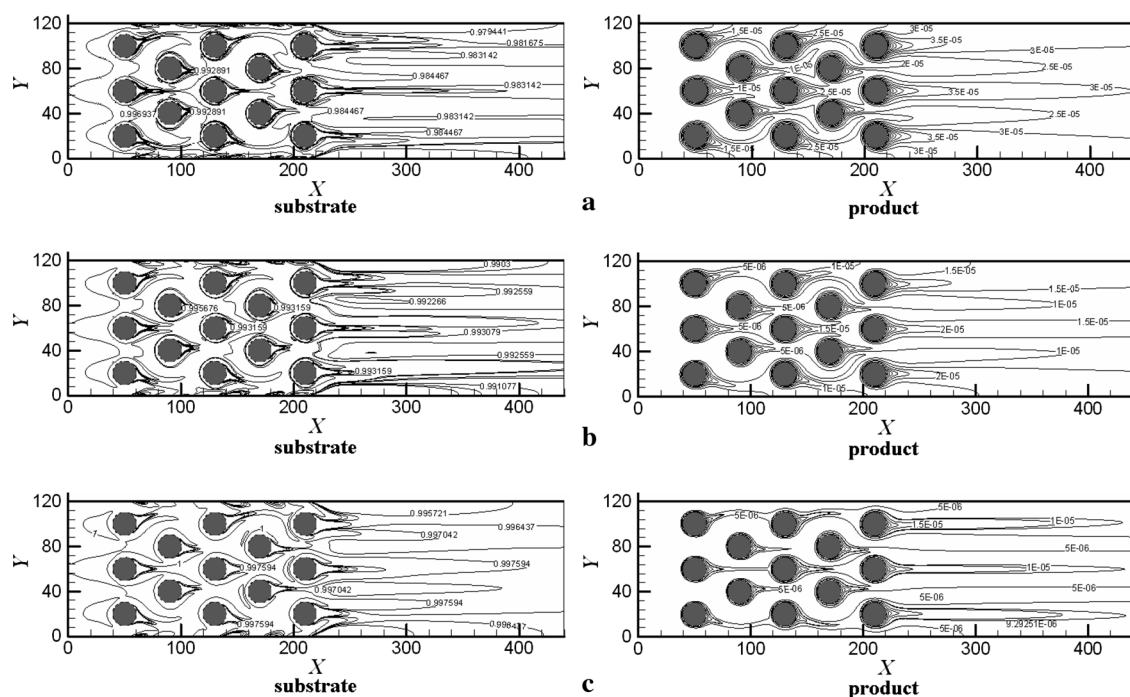


**Fig. 8** Concentration contours of substrate and hydrogen product for fluid flow around staggered cylinder bundle with cylinder spacing  $S = 2.0$  for **a**  $Re = 0.14$ , **b**  $Re = 0.28$  and **c**  $Re = 0.56$

$Re$  number, owing to high fluid velocity and short HRT. It is obviously noted from the comparison with the inline arrangement case in Fig. 6 that the largest velocity between cylinders in the staggered arrangement case is much higher (cf. Figs. 6a, 9a), and the concentration difference between the front and back points of cylinders is larger at a given  $Re$  number (cf. Figs. 6b, 9b), obviously seen in the product profile along channel centerline. It can be concluded that the staggered arrangement strengthens the fluid disturbance between cylinders and increases the concentration gradient on reaction surfaces, consequently, enhancing the mass transfer and bioreaction.

Based on the simulation results, the average drag coefficient, Sherwood number and consumption efficiency of the substrate flow around cylinders are also evaluated, as shown in Table 2. For a specific cylinder spacing, the drag coefficient and substrate consumption efficiency decrease with an increase in  $Re$  number, while the Sherwood number increases; for a specific  $Re$  number, all the drag coefficient, Sherwood number and consumption efficiency increase with decreasing cylinder spacing. These features are the result from the effect of flow interaction and variation of inlet substrate load, which is similar to the analysis for that in the inline bundle. However, some differences are easily noted from comparison of Tables 1 and 2. The drag coefficient, the Sherwood number and the consumption efficiency for glucose solution flow around the staggered bundles is higher than that of flow around the inline

bundles at a same condition. However, the increment in  $C_d$  (comparing the two bundle arrangements) is minished with increasing  $Re$  number as well as cylinder spacing and is less than 1 % for all cases. While the increment in the Sherwood number is enlarged with increasing  $Re$  number as well as decreasing cylinder spacing and is much larger than that in drag coefficient, even reached up to 30 %. The increment in the substrate consumption efficiency might be ignored at large cylinder spacing and reaches the maximum value of 12 % at  $S = 2.0$  and  $Re = 0.56$ . In conclusion, the choosing of staggered cylinder bundle is beneficial to the biochemical reaction, and improves the Sherwood number and substrate consumption efficiency.

## 6 Conclusion

The lattice Boltzmann method is used to simulate the flow and mass transport of glucose solution flow around cylinder bundle attached with PSB biofilm for biohydrogen production. The effects of cylinder spacing,  $Re$  number and cylinder bundle arrangement are investigated. The flow and concentration fields of the substrate and product are determined under various conditions, showing that slight fluid disturbance can induce great influence on mass transfer. The concentration boundary layer of the glucose and hydrogen experiences a minification with increasing  $Re$  number and decreasing cylinder spacing, and it is

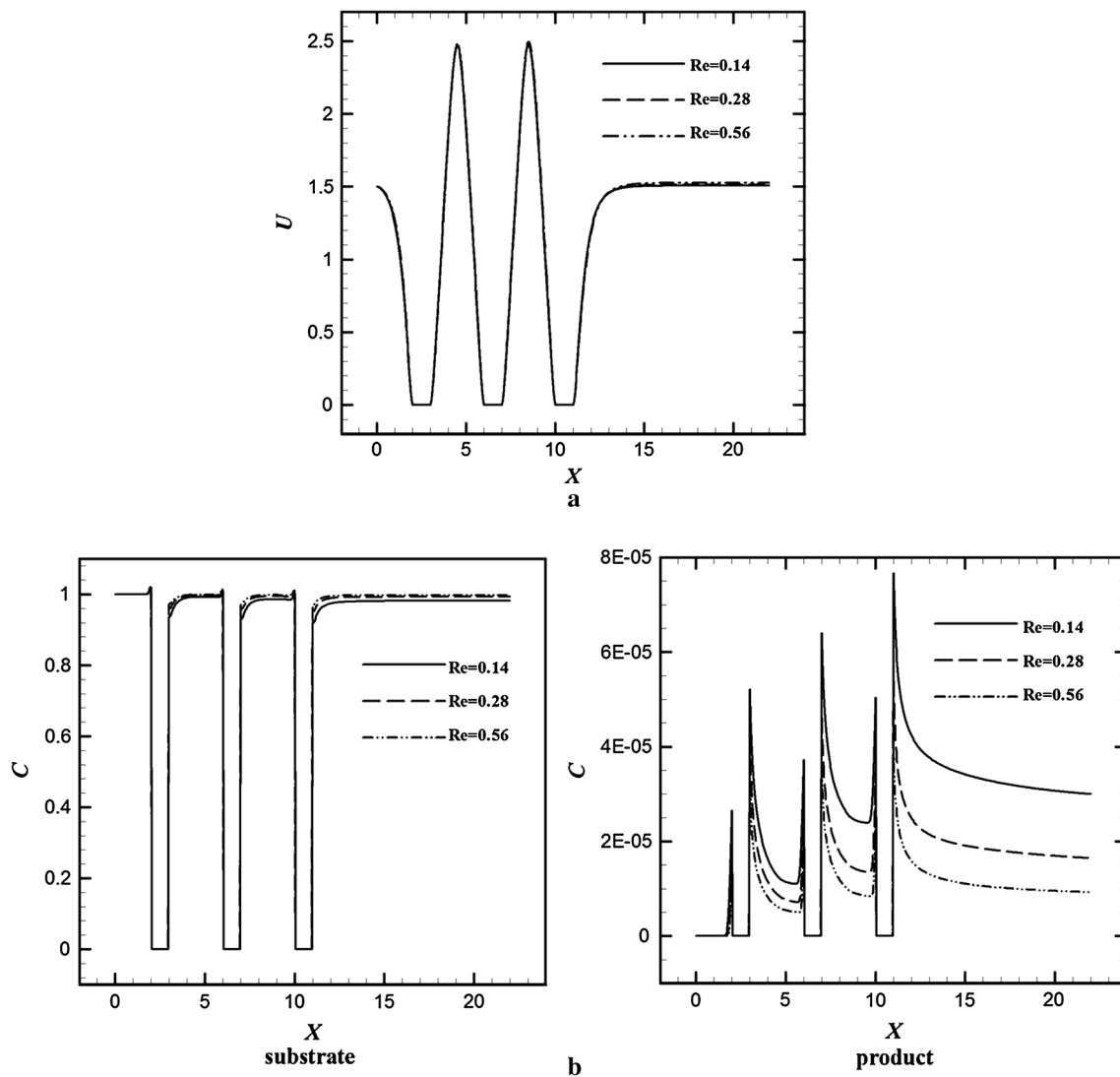


**Fig. 9** Comparison of **a** velocity and **b** concentration profiles along channel centerline of fluid flow around staggered cylinder trundles with cylinder spacing  $S = 2.0$  for  $Re = 0.14, 0.28$  and  $0.56$

**Table 2** The effects of  $Re$  number and cylinder spacing  $S$  on drag coefficient, Sherwood number and consumption efficiency of substrate for fluid flow around staggered cylinder bundles

$Re$	$C_d$			$Sh$			$\eta$ (%)		
	0.14	0.28	0.56	0.14	0.28	0.56	0.14	0.28	0.56
$S$									
1.5	2,454.58	1,244.74	640.78	0.081	0.150	0.303	0.583	0.536	0.528
2.0	865.87	434.99	219.71	0.037	0.069	0.131	0.537	0.507	0.492
3.0	411.40	206.25	103.92	0.021	0.039	0.075	0.463	0.419	0.410

thinner for the flow in staggered bundles, compared with the flow in inline bundles, which increases the velocity and concentration gradients around cylinders and enhances the mass transfer and bioreaction. Furthermore, the staggered arrangement leads to an up to 30 % increment in Sherwood number, but a less than 1 % increment in drag coefficient

under a given condition. The total amount of the substrate consumption per cylinder's surface in the bioreactor increase with increasing  $Re$  number and decreasing cylinder spacing, while the maximum substrate consumption efficiency is reached at the small cylinder spacing and low solution velocity due to long hydraulic retention.

**Acknowledgments** The authors would like to acknowledge the joint support of National Science Fund for Distinguished Young Scholars (No. 50825602), National Natural Science Foundation of China (No. 51136007, 20876183), the Fundamental Research Funds for the Central Universities (No. CDJXS 10142223).

## References

- Kapdan IK, Kargi F (2006) Bio-hydrogen production from waste materials. *Enzyme Microb Technol* 38:569–582
- Goltsov VA, Veziroglu TN, Goltsova LF (2006) Hydrogen civilization of the future—A new conception of the IAHE. *Int J Hydrogen Energy* 31:153–159
- Chen CY, Chang JS (2006) Enhancing phototropic hydrogen production by solid-carrier assisted fermentation and internal optical-fiber illumination. *Process Biochem* 41:2041–2049
- Lin CN, Wu SY, Chang JS (2006) Fermentative hydrogen production with a draft tube fluidized bed reactor containing silicone-gel-immobilized anaerobic sludge. *Int J Hydrogen Energy* 31:2200–2210
- Zhang ZP, Show KY, Tay JH, Liang DT, Lee DJ (2008) Biohydrogen production with anaerobic fluidized bed reactors—a comparison of biofilm-based and granule-based systems. *Int J Hydrogen Energy* 33:1559–1564
- Tian X, Liao Q, Zhu X, Wang Y, Zhang P, Li J, Wang H (2010) Characteristics of a biofilm photobioreactor as applied to photohydrogen production. *Bioresour Technol* 101:977–983
- Wang YZ, Liao Q, Zhu X, Tian X, Zhang C (2010) Characteristics of hydrogen production and substrate consumption of *Rhodospseudomonas palustris* CQK 01 in an immobilized-cell photobioreactor. *Bioresour Technol* 101:4034–4041
- Zhang C, Zhu X, Liao Q, Wang Y, Li J, Ding Y, Wang H (2010) Performance of a groove-type photobioreactor for hydrogen production by immobilized photosynthetic bacteria. *Int J Hydrogen Energy* 35:5284–5292
- Liao Q, Liu DM, Ye DD, Zhu X, Lee DJ (2011) Mathematical modeling of two-phase flow and transport in an immobilized-cell photobioreactor. *Int J Hydrogen Energy* 36:13939–13948
- Das D, Badri PK, Kumar N, Bhattacharya P (2002) Simulation and modeling of continuous H<sub>2</sub> production process by *Enterobacter cloacae* IIT-BT 08 using different bioreactor configuration. *Enzyme Microb Technol* 31:867–875
- Chang C, Liu CH, Lin CA (2009) Boundary conditions for lattice Boltzmann simulations with complex geometry flows. *Comput Math Appl* 58:940–949
- Pomeau Y (2007) 20 years of lattice dynamics: a personal view. *Int J Mod Phys C* 18:437
- Raabe D (2004) Overview of the lattice Boltzmann method for nano- and microscale fluid dynamics in materials science and engineering. *Model Simul Mater Sci Eng* 12:R13
- Dupin MM, Halliday I, Care CM, Alboul L, Munn LL (2007) Modeling the flow of dense suspensions of deformable particles in three dimensions. *Phys Rev E* 75:066707
- Kebllinski P, Phillpot SR, Choi SUS, Eastman JA (2002) Mechanisms of heat flow in suspensions of nano-sized particles (nanofluids). *Int J Heat Mass Transf* 45:855–863
- He X, Chen S, Zhang R (1999) A lattice Boltzmann scheme for incompressible multiphase flow and its application in simulation of Rayleigh–Taylor instability. *J Comput Phys* 152:642–663
- Shan X, Chen H (1993) Lattice Boltzmann model for simulating flows with multiple phases and components. *Phys Rev E* 47:1815
- Yang ZL, Dinh TN, Nourgaliev RR, Sehgal BR (2001) Numerical investigation of bubble growth and detachment by the lattice-Boltzmann method. *Int J Heat Mass Transf* 44:195–206
- Gabrielli A, Succi S, Kaxiras E (2002) A lattice Boltzmann study of reactive microflows. *Comput Phys Commun* 147:516–521
- Tian Z-W, Zou C, Liu H-J, Guo Z-L, Liu Z-H, Zheng C-G (2007) Lattice Boltzmann scheme for simulating thermal micro-flow. *Phys A* 385:59–68
- Li Q, Zhao K, Xuan YM (2011) Simulation of flow and heat transfer with evaporation in a porous wick of a CPL evaporator on pore scale by lattice Boltzmann method. *Int J Heat Mass Transf* 54:2890–2901
- Yan YY, Zu YQ (2008) Numerical simulation of heat transfer and fluid flow past a rotating isothermal cylinder—a LBM approach. *Int J Heat Mass Transf* 51:2519–2536
- Jeong N, Choi DH, Lin CL (2008) Estimation of thermal and mass diffusivity in a porous medium of complex structure using a lattice Boltzmann method. *Int J Heat Mass Transf* 51:3913–3923
- Onishi J, Chen Y, Ohashi H (2006) Dynamic simulation of multi-component viscoelastic fluids using the lattice Boltzmann method. *Phys A* 362:84–92
- Shan X, Doolen G (1996) Diffusion in a multicomponent lattice Boltzmann equation model. *Phys Rev E* 54:3614
- Verma N, Mewes D, Luke A (2010) Lattice Boltzmann study of velocity, temperature, and concentration in micro-reactors. *Int J Heat Mass Transf* 53:3175–3185
- Yu X, Shi B (2006) A lattice Boltzmann model for reaction dynamical systems with time delay. *Appl Math Comput* 181:958–965
- Sullivan SP, Sani FM, Johns ML, Gladden LF (2005) Simulation of packed bed reactors using lattice Boltzmann methods. *Chem Eng Sci* 60:3405–3418
- Sullivan SP, Gladden LF, Johns ML (2006) 3D chemical reactor LB simulations. *Math Comput Simul* 72:206–211
- FlekkZy EG (1993) Lattice Bhatnagar–Gross–Krook models for miscible fluids. *Phys Rev E* 47:4247
- Qian YH, d’Humières D, Lallemand P (1992) Lattice BGK models for Navier–Stokes equation. *Europhys Lett* 17:479
- He X, Luo LS (1997) A priori derivation of the lattice Boltzmann equation. *Phys Rev E* 55:6333–6336
- He X, Luo LS (1997) Theory of the lattice Boltzmann method: from the Boltzmann equation to the lattice Boltzmann equation. *Phys Rev E* 56:6811
- Guo Z, Shi B, Wang N (2000) Lattice BGK model for incompressible Navier–Stokes equation. *J Comput Phys* 165:288–306
- Guo Z, Zheng C, Shi B (2002) An extrapolation method for boundary conditions in lattice Boltzmann method. *Phys Fluids* 14:2007
- Kang XY, Liao Q, Zhu X, Yang YX (2010) Non-equilibrium extrapolation method in the lattice Boltzmann simulations of flows with curved boundaries (non-equilibrium extrapolation of LBM). *Appl Therm Eng* 30:1790–1796
- Yang YX, Liao Q, Zhu X, Wang H, Wu R, Lee DJ (2011) Lattice Boltzmann simulation of substrate flow past a cylinder with PSB biofilm for bio-hydrogen production. *Int J Hydrogen Energy* 36:14031–14040
- He X, Doolen G (1997) Lattice Boltzmann method on curvilinear coordinates system: flow around a circular cylinder. *J Comput Phys* 134:306–315
- Mei R, Yu D, Shyy W, Luo LS (2002) Force evaluation in the lattice Boltzmann method involving curved geometry. *Phys Rev E* 65:041203
- Obeid J, Magnin JP, Flaus JM, Adrot O, Willison JC, Zlatev R (2009) Modelling of hydrogen production in batch cultures of the photosynthetic bacterium *Rhodobacter capsulatus*. *Int J Hydrogen Energy* 34:180–185
- Schäfer M, Turek S (1996) Benchmark computations of laminar flow around a cylinder. In: Hirschel EH (ed) *Flow simulation with high-performance computers II, Notes in numerical fluid mechanics*, vol 52. Vieweg, Braunschweig, pp 547–566

42. Feng ZG, Michaelides EE (2002) Interparticle forces and lift on a particle attached to a solid boundary in suspension flow. *Phys Fluids* 14:49–60
43. Ladd AJC (1994) Numerical simulations of particulate suspensions via a discretized Boltzmann equation. Part 1. Theoretical foundation. *J Fluid Mech* 271:285–309
44. Ladd AJC (1994) Numerical simulations of particulate suspensions via a discretized Boltzmann equation. Part 2. Numerical results. *J Fluid Mech* 271:311–339